Journal of Materials Chemistry A

ROYAL SOCIETY OF CHEMISTRY

PAPER

View Article Online
View Journal | View Issue

Check for updates

Cite this: *J. Mater. Chem. A*, 2025, **13**, 30140

Synergistic passivation and stable carrier transport enable efficient blade-coated perovskite solar cells fabricated in ambient air

Jian-An Li,†[a] Hailong Ma, †[b] Xiangpeng Ding,[b] Shuoren Li, [a] Bin Han,[a] Wangxian Chen,[a] Sihao Huang,[a] Shuyan Chen,[a] Yuelin Kuang,[a] Zixi Liu[a] and Chang Yan *[acde]

Perovskite solar cells (PSCs) continue to grapple with efficiency and long-term stability limitations stemming from crystalline defects (such as halide vacancies, undercoordinated Pb^{2+} defects, *etc.*) and interfacial energy-level misalignments. To mitigate these challenges, we design and introduce Bis(3-fluorophenyl) disulfide (SF) as a multifunctional interfacial modifier at the perovskite (PVK) and electron transport layer (ETL) interface. The SF molecule engages in a dual-site synergistic passivation mechanism: sulfur atoms form robust Pb–S bonds with undercoordinated Pb^{2+} ions, while fluorine atoms occupy iodine vacancies and form hydrogen bonds with FA^+/MA^+ cations. This dual interaction suppresses ion migration and halide volatilization, significantly reducing surface defect density and trap states, thereby improving carrier transport. Stroboscopic scattering microscopy (stroboSCAT) reveals superior long-term carrier dynamics in SF-treated films, which retain ~86% of their initial maximum carrier diffusion coefficient after 2000 hours in ambient air, far surpassing control devices (~41%). Notably, after three months of ambient storage, SF-modified perovskite film exhibits an approximately threefold higher average carrier diffusion coefficient (0.0247 ± 0.0028 cm^2 s^{-1}) than the control group (0.0079 ± 0.0017 cm^2 s^{-1}), underscoring perovskite film quality enhancement. This sustained diffusion coefficient improvement directly correlates with elevated device stability and performance retention. Correspondingly, blade-coated PSCs incorporating SF, fabricated under ambient conditions, reach a peak power conversion efficiency (PCE) of 24.60% with an open-circuit voltage (V_{oc}) of 1.17 V. Furthermore, the hydrophobic

Received 12th June 2025
Accepted 1st August 2025

DOI: 10.1039/d5ta04703j

rsc.li/materials-a

[a]*Sustainable Energy and Environment Thrust, Function Hub, The Hong Kong University of Science and Technology (Guangzhou), Guangzhou, Guangdong, 511400, P. R. China. E-mail: changyan@hkust-gz.edu.cn*

[b]*Advanced Materials Thrust, Function Hub, The Hong Kong University of Science and Technology (Guangzhou), Guangzhou, Guangdong, 511400, P. R. China*

[c]*Carbon Neutrality and Climate Change Thrust, Society Hub, The Hong Kong University of Science and Technology (Guangzhou), Guangzhou, Guangdong, 511400, P. R. China*

[d]*Guangdong-Hong Kong Joint Laboratory for Carbon Neutrality, Jiangmen Laboratory of Carbon Science and Technology, Jiangmen 529199, Guangdong Province, China*

[e]*Department of Electronic and Computer Engineering, The Hong Kong University of Science and Technology, Hong Kong, SAR, 999077, P. R. China*

† These authors contributed equally to this work.

Chang Yan

Dr Chang Yan has been an Assistant Professor in the Sustainable Energy and Environment Thrust at Hong Kong University of Science and Technology (Guangzhou) since 2022. He was awarded PhD degree in Photovoltaic Engineering from UNSW in 2017, supervised by Prof. Martin A. Green and Xiaojing Hao. Then he works as a postdoc and lecturer at UNSW before his appointment at HKUST(GZ). His current research interest focuses on the use Artificial Intelligence and automation-robot to develop next-generation ultra-high efficiency tandem solar cells and flexible & transparent solar cells based on the perovskite, kesterite & chalcopyrite. He was included in the top 2% list of global applied physics scientists assessed by standardized citation metrics in the single year of 2024.

nature of SF's fluorinated aromatic rings provides an effective barrier against moisture, enabling devices to maintain 96.8% of their initial PCE after 2000 hours under 30–40% relative humidity, far exceeding the control's 60% (after 1200 hours) retention. Collectively, these findings demonstrate that SF enables a robust, scalable strategy for concurrently enhancing efficiency and environmental durability in PSCs, while also offering valuable molecular design insights for future multifunctional interfacial engineering using bidentate passivating agents.

Introduction

Perovskite has emerged as a leading contender in next-generation photovoltaics due to its exceptional optoelectronic properties, including high absorption coefficients, long carrier diffusion lengths, and bandgap tunability.[1–5] With solution-processable fabrication at low temperatures, perovskites offer a scalable pathway toward cost-effective utilization of solar energy.[6] The record certified power conversion efficiency (PCE) of single-junction perovskite solar cells (PSCs) has exceeded 27%,[1] making them highly competitive with traditional silicon technologies. However, this peak performance is typically achieved under well-protected inert conditions (*e.g.*, glovebox fabrication), which raises cost and scalability concerns.[7–9] To transition perovskite technology toward commercial viability, it is critical to develop efficient ambient fabrication techniques, such as air-blade coating. Although this method has yielded efficiencies up to 25%,[10] films produced under ambient conditions are more susceptible to defects that impair carrier transport and device stability.[11]

The performance and longevity of PSCs are fundamentally tied to charge carrier dynamics within the perovskite layer.[12,13] Efficient carrier diffusion ensures that photo-generated electrons and holes can traverse the film without encountering non-radiative recombination centers, maximizing light harvesting and charge extraction.[14,15] Unfortunately, the polycrystalline nature of perovskite films, especially those processed in ambient conditions, makes them vulnerable to grain boundaries, vacancies, and interfacial defects that trap carriers and accelerate ionic migration.[16–25] These defects, such as uncoordinated Pb^{2+} sites[26] and halide or organic cation vacancies, not only diminish carrier diffusion coefficient but also initiate degradation pathways, limiting long-term operational stability. Hence, defect passivation has become a focal strategy in PSC research.[8,27,28] Among various passivation approaches, the use of multifunctional molecules capable of addressing both shallow and deep traps simultaneously presents a promising route to boost both device efficiency and stability.[16,29,30]

In this study, we report a dual-site synergistic defect passivation strategy using bis(3-fluorophenyl) disulfide (SF), a multifunctional small molecule featuring both sulfur and fluorine atoms. The sulfur atoms in SF form strong coordination bonds with undercoordinated Pb^{2+}, yielding robust Pb–S interactions, while the fluorine atoms fulfill a dual role: they passivate halide vacancies and form hydrogen bonds with FA^+/MA^+ organic cations, thereby suppressing cation volatilization. Furthermore, the aromatic fluorinated structure acts as a hydrophobic barrier, significantly enhancing resistance to environmental degradation. To elucidate the impact of SF on carrier dynamics, we employ stroboSCAT, a non-invasive, time-resolved optical technique capable of visualizing carrier diffusion with nanometer spatial and sub-nanosecond temporal resolution.[31] SF-modified films exhibit notably enhanced carrier transport properties, with a sustained long-term carrier diffusion coefficient. Strikingly, after 2000 h of storage under ambient conditions, the average carrier diffusion coefficient of SF-treated devices increased by a factor of ~3 (from 0.0079 ± 0.0017 cm^2 s^{-1} to 0.0247 ± 0.0028 cm^2 s^{-1}), underscoring the intrinsic improvements in film quality and defect passivation stability over time. This exceptional enhancement in charge transport directly contributes to the superior device performance, as demonstrated by a certified power conversion efficiency (PCE) of 24.60% and a high open-circuit voltage (V_{oc}) of 1.17 V. These findings highlight the critical role of interfacial molecular engineering in optimizing charge dynamics and stability, offering a promising pathway toward the development of highly efficient and durable perovskite solar cells.

Results and discussion

Fig. 1a shows the molecular structure of bis(3-fluorophenyl) disulfide (SF), which consists of two phenyl rings connected by a disulfide bond, with one fluorine atom attached to each phenyl ring. This molecule is utilized for passivating the surface defects as well as modifying the PVK/ETL interface (Fig. 1b). To investigate the effect of SF interface modification on the photovoltaic performance of the devices, the light *J–V* curves of PSCs treated with different concentrations of SF were recorded (Fig. S3 and S4). The experimental results indicate that the optimal concentration of SF is 0.50 mg mL^{-1}. The specific photovoltaic parameters optimized for this concentration are recorded in Table S1. For ease of comparison, subsequent characterization tests related to SF were conducted under the aforementioned optimal conditions.

First, the interaction between SF molecules and perovskite was analyzed using X-ray photoelectron spectroscopy (XPS). As observed in Fig. 1e, the peaks at 140.1 and 145.0 eV for the control perovskite film correspond to the Pb $4f_{7/2}$ and Pb $4f_{5/2}$ levels,[32] respectively. Upon the introduction of SF molecules to the film surface, the Pb 4f peaks exhibited varying degrees of shift towards lower binding energy, specifically to 138.9 and 143.8 eV, respectively. The shift of the Pb 4f peaks towards lower binding energy for the passivated films can be attributed to the highly electronegative F atoms occupying the I vacancies in the perovskite lattice, re-establishing coordination with Pb^{2+} ions. Additionally, this shift can also be attributed to the S atoms in the disulfide bonds contributing their lone pair electrons to the empty orbitals of Pb^{2+}, forming Pb–S coordination bonds that

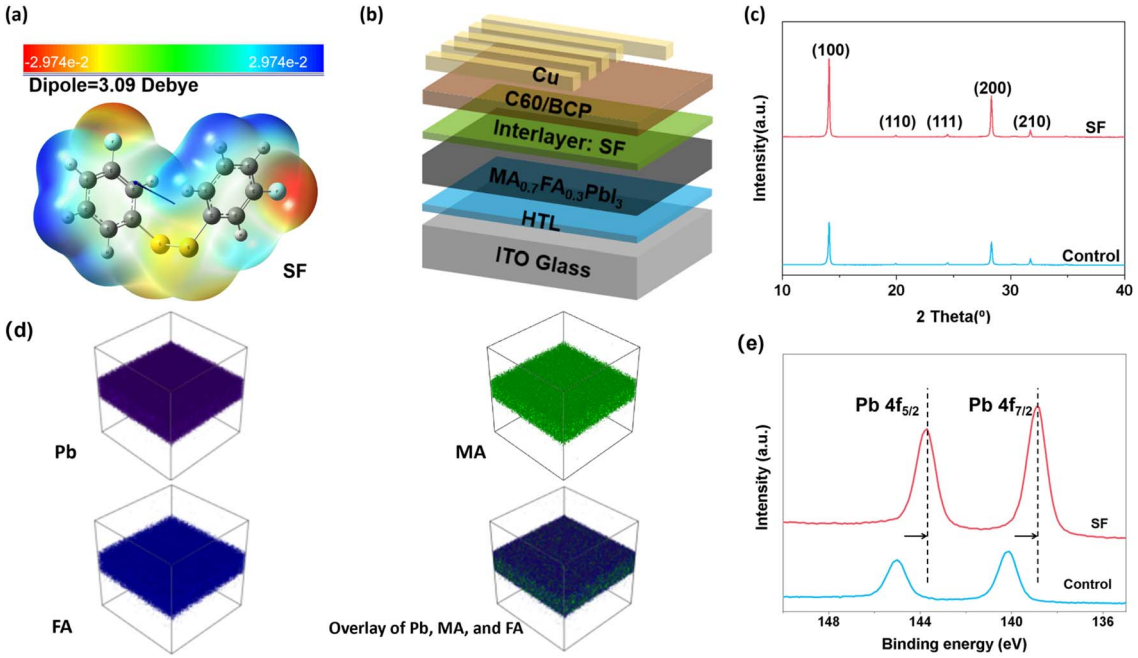

Fig. 1 (a) The electrostatic potential (as shown in the color bar, unit: a.u.), dipole moments and molecular structure of SF. (b) Schematic illustration of a perovskite solar cell with a post-treated SF passivation between perovskite and C_{60} layers. (c) XRD patterns for the control and SF-treated perovskite films. (d) 3D form TOF-SIMS spectra of SF-treated PVK films. (e) XPS spectra of the control and SF-treated perovskite films.

anchor the Pb^{2+} defects.[33,34] It is speculated that the synergistic effect between the fluorine atoms and the disulfide bonds results in a stronger passivation effect. Meanwhile, the energy dispersive spectroscopy (EDS) characterization of perovskite film to verify the inclusion of SF, as shown in Fig. S5, the distribution of S and F elements on the perovskite film surface is homogeneous.[30] This result reveals S and F elements distributed throughout the perovskite interface. Fourier-transform infrared (FT-IR) spectroscopy was performed to confirm the coordination effect. In Fig. S6, the C=N stretching vibration of FA^+, originally observed at 1716 cm^{-1}, shifts to 1712 cm^{-1} upon addition of SF.[35] The shifts indicate that SF molecule enhances hydrogen bonding with FA^+.

In order to better grasp the electron density distribution, the electrostatic potential (ESP) of the molecule SF was analyzed by the density functional theory method.[36] As shown in Fig. 1a, the negative ESP (reddish-orange region) is mainly distributed on the –F group due to its strong electron-withdrawing property, which is beneficial for the coordination with the under-coordinated Pb^{2+} ions.[8] Meanwhile, the highly electronegative disulfide group induces the electron to run away from the benzene ring, in turn, presenting a positive ESP (blue region) on the benzene ring. This uneven electron distribution is quantified by a large dipole moment in the direction of the disulfide bond by calculations. This large molecular polarity with a strong electron delocalization further enhances the interaction between SF and undercoordinated Pb^{2+} ions.[36,37]

Through time-of-flight secondary ion mass spectrometry (TOF-SIMS) testing, it was observed (Fig. 1d and S7) that the control group devices exhibited an outward migration of FA^+ at the top of the perovskite layer.[14,38] In contrast, the SF-treated devices did not show this phenomenon: the distribution of the components $MA_{0.7}FA_{0.3}PbI_3$ in the SF-treated perovskite layer, including MA^+, FA^+, and Pb^{2+}, was very uniform. This could be attributed to the coordination effects of the highly electronegative fluorine atoms and the lone pair electrons from the disulfide groups in the SF molecules, which effectively suppress the volatilization and migration of iodide ions and organic cations through dual-site synergistic passivation of deep and shallow defects at the surface of the perovskite.

From XRD patterns (Fig. 1c), no systematic peak shifts relative to the control film were observed, indicating the identical crystal structure of perovskite. The main peak (100) for the SF-treated film becomes stronger and sharper, reflecting either an expansion of the mean size of perovskite crystallites or a reduction in crystal disorders/defects. The superior photovoltaic performance observed in devices incorporating the (100) facet can be attributed to its favorable electronic properties, including higher charge carrier diffusion coefficient, reduced density of trap states, and decreased exciton binding energy, which collectively facilitate more efficient charge transport and extraction.[39]

Based on the aforementioned characterization and analysis, the schematic diagram of the interaction between SF and perovskite is illustrated in Fig. 2a. The synergistic effects of the two functional groups in SF can be summarized as follows: the sulfur atoms with lone pair electrons on the disulfide bond of SF can anchor to uncoordinated Pb^{2+} in the perovskite lattice, forming Pb–S coordination bonds (denoted as III in the figure). The highly electronegative fluorine atoms can, on one hand, fill the I vacancy defects (denoted as I in the figure), anchoring uncoordinated Pb^{2+} in the perovskite lattice to form Pb–F

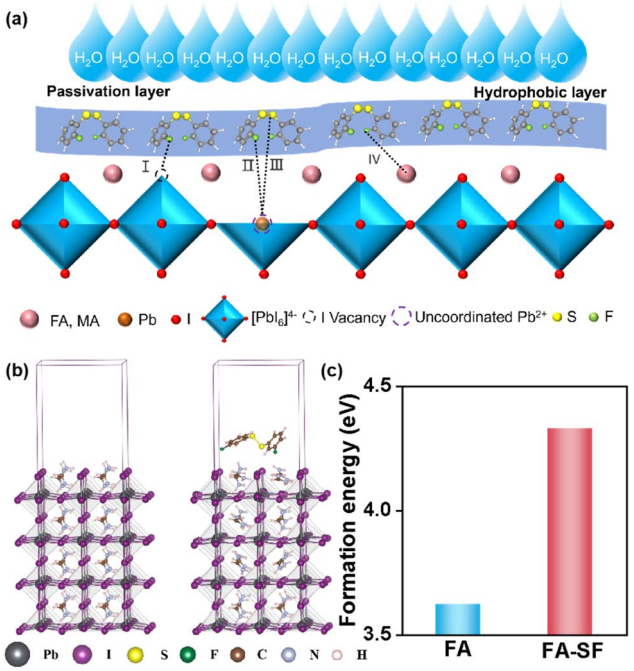

Fig. 2 (a) Schematic illustration of the interaction between SF and perovskite (partial magnification of I, II, III, and IV). (b) Optimized structures of the $FAPbI_3$ surface (left) and a SF molecule (right) adjacent to the $FAPbI_3$ surface. (c) Formation energy of a surface FA vacancy in the clean $FAPbI_3$ (FA), and in the SF (FA-SF) species incorporated surfaces.

coordination bonds (denoted as II in the figure). On the other hand, they can also form hydrogen bonds with organic cations such as FA^+/MA^+ (denoted as IV in Fig. 2a, with theoretical calculation results illustrated in Fig. 2b), effectively suppressing ion migration. The two functional groups could work synergistically to passivate both deep and shallow defects at the surface and grain boundaries of the perovskite.[40–42] Furthermore, the fluorinated compounds exhibit excellent moisture resistance and thermal stability (with the water contact angles of PVK films rising markedly from 72.0° to 85.2°, see Fig. S8), which can enhance the long-term stability of the films and the corresponding devices.

The introduction of SF modifies local surface bonding, inducing a reorientation of FA^+ cations toward –F to maximize N–H···F hydrogen bonding (Fig. 2b). This strong fluoride–organic cation interaction markedly stabilizes the perovskite surface.[38] Therefore, SF incorporation raises the formation energy (Fig. 2c) of FA vacancies from 3.62 eV to 4.33 eV, demonstrating its role in suppressing vacancy generation. These effects collectively explain the enhanced stability of SF-treated perovskite films.

To directly investigate the passivation effect of SF molecules on the perovskite layer and the carrier transport dynamics, Photoluminescence (PL) and time-resolved photoluminescence (TRPL) tests were conducted (sample configuration: glass/ITO/Poly-4PACz/PVK/with or without SF). As observed in Fig. 3g, the fluorescence intensity of the perovskite films significantly increases after surface modification, indicating a reduction in nonradiative recombination within the films. The fluorescence peak position of SF-modified perovskite films shifts from 808 to 791 nm, indicating the radiative process may shift from band-to-defects to possible band-to-band radiative recombination due to passivated shallow and deep traps (defects) by SF

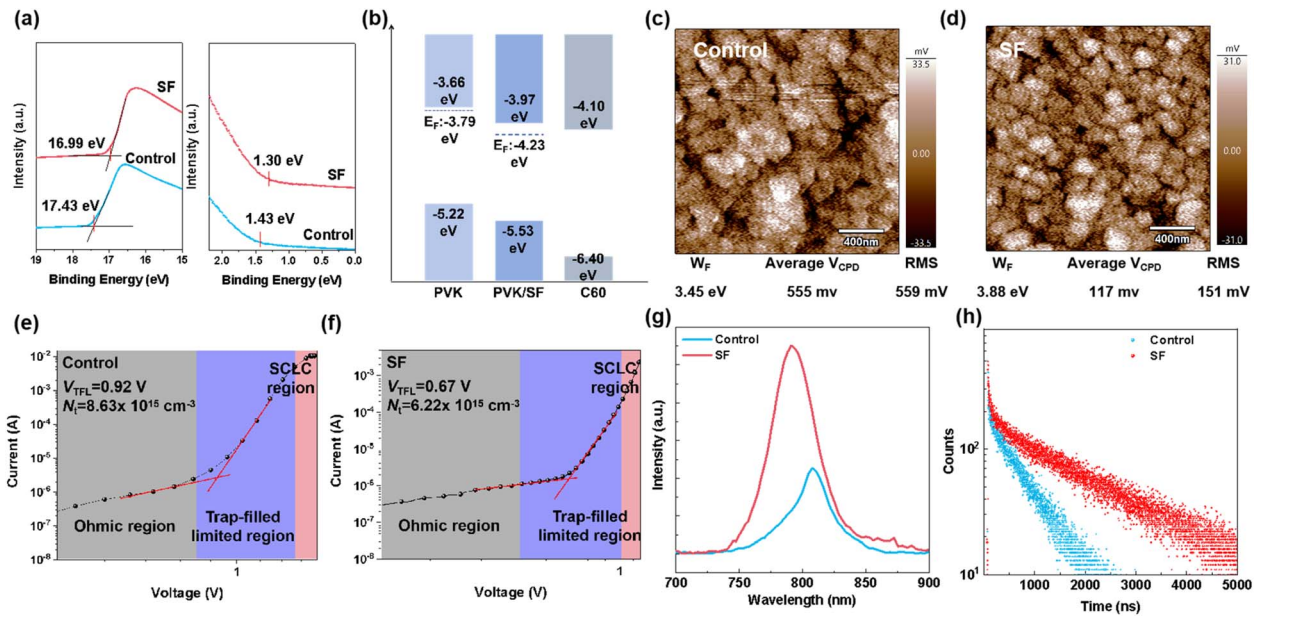

Fig. 3 (a) UPS spectra of control, SF-treated perovskite films' surfaces. (b) Energy level scheme for the control, SF-treated perovskite films' surfaces extracted from UPS data. (c) flatten KPFM images of the perovskite films without and (d) with SF surface treatment (with the structure of glass/ITO/Poly-4PACz/PVK and glass/ITO/Poly-4PACz/PVK/SF, respectively) with the extracted work function and average Contact Potential Difference (V_{CPD}), Root Mean Square (RMS) of V_{CPD}. (e) Dark J–V curves of the control and (f) SF-treated PVK with the structure of glass/ITO/SnO_2/PVK/C_{60}/Cu and glass/ITO/SnO_2/PVK/SF/C_{60}/Cu, respectively. (g) Steady-state and (h) time-resolved PL spectra for the control and SF-treated perovskite films with the structure of glass/ITO/Poly-4PACz/PVK and glass/ITO/Poly-4PACz/PVK/SF, respectively.

molecules. The SF-modified perovskite shows PL intensity 2.43 times compared to that of the control sample, showing the decent effectiveness of using SF to passivate the defects and suppress the non-radiative recombination. Combined with the essentially unchanged absorption edge in the UV-vis absorption spectra (Fig. S9), this blue shift suggests a reduction in band tail states within the perovskite. From the TRPL decay curves shown in Fig. 3h, it is evident that all modified perovskite films exhibit a markedly extended carrier lifetime τ_{avg}. The TRPL decay curves were fitted using a biexponential model, with the fitting parameters summarized in Table S2. The average lifetime τ_{avg} for the SF-treated films is 1691.0 ns, which is 2.6 times longer than the 662.6 ns observed for the control films. The increased carrier lifetime in the SF-modified films compared to the control films indicates a significant improvement in film quality, with a reduction in nonradiative recombination sites within the films. In summary, the passivation process effectively suppresses interfacial nonradiative recombination processes, thereby enhancing the overall performance of the perovskite films. The average lifetime τ_{avg} reflects the overall recombination processes, where τ_1 corresponds to surface recombination and τ_2 corresponds to bulk recombination. The ratio of τ_1 and τ_2 in SF-treated PVK film decreased significantly (Table S2), indicating that the surface non-radiative recombination was reduced, which was also consistent with the increase of PLQY (see Fig. S12 and Table S3) at the interface.[43]

Optimal energy level alignment plays a critical role in determining device performance. To systematically characterize the electronic structure, ultraviolet photoelectron spectroscopy (UPS) measurements were conducted to precisely determine the valence band energy levels of the different PVK thin-film samples.

Compared to the control film, the valence band maximum (VBM) of the SF-treated film decreases from −5.22 eV to −5.53 eV, while the work function (W_F) changes from 3.79 eV to 4.23 eV. The energy level diagram of the perovskite thin films' surfaces is illustrated in Fig. 3a and b. The downward shift of the VBM results in a more favorable energy level alignment at the PVK/C_{60} interface, which can reduce the interface non-radiative recombination and enhance the open-circuit voltage of the device.[44–47]

As shown in Fig. S10, the AFM results indicate that surface modification leads to a lower surface roughness. Compared to the control film with a roughness (R_a) of ∼8 nm, the SF-treated film is reduced to ∼6 nm. The decreased surface roughness improves interfacial contact, demonstrating that SF post-treatment produces a smoother and more homogeneous surface, which enhances carrier extraction and transport efficiency.[48]

Furthermore, Kelvin probe force microscopy (KPFM) was employed to analyze the surface potential distribution of PVK films. The surface potential was quantified by measuring the electrostatic interaction between the conductive atomic force microscopy (AFM) tip and the film surface. A reduction in V_{CPD} corresponds to an increase in the W_F of the surface, indicative of diminished n-type defects at the film interface.[49] The spatial variation of surface potential across the KPFM-mapped regions is illustrated in Fig. 3c and d. Notably, the SF-treated sample exhibited a significantly lower V_{CPD} (117 mV on average) compared to the untreated control film (555 mV on average), along with a reduced RMS surface potential fluctuation (from 559 mV to 151 mV; see Fig. S8). These findings suggest that SF treatment effectively suppresses n-type contributing defects and enhances surface homogeneity in PVK films.[50–52] Furthermore, the W_F differences between the two samples, as derived from UPS spectral analysis (0.440 eV), exhibit excellent consistency with the corresponding values obtained *via* KPFM measurements (0.438 eV).[53] This strong correlation between independent characterization techniques further validates the reliability and accuracy of the experimental data.

Owing to its strong dipole moment (3.09 debye, Fig. 1a), SF is more likely to induce a stable interfacial dipole layer at the PVK/C_{60} interface, which enhances carrier transport, thereby facilitating enhanced electron transport at the PVK/C_{60} interface.[54] Consequently, the dual-site passivation effect of SF promotes a more uniform surface potential distribution across the PVK layer. The observed reduction in surface potential heterogeneity and improved morphological uniformity imply a decrease in defect density, which is expected to enhance charge transfer efficiency at adjacent charge-selective contacts.

To evaluate the trap density of the PVK films, we performed space-charge limited current (SCLC) measurements using a glass/ITO/SnO_2/PVK/C_{60}/Cu device structure. The corresponding dark *J–V* characteristics are presented in Fig. 3e and f. The trap density (N_t) was calculated using the following equation:[55]

$$N_t = \frac{2V_{TFL}\varepsilon_r\varepsilon_0}{qL^2}$$

where L is the thickness of the perovskite film, q is the elementary charge, ε_r is the relative dielectric constant of the perovskite, and ε_0 is the vacuum permittivity. The trap-filled limit voltage (V_{TFL}) corresponds to the transition point between the low-bias ohmic response and the high-bias exponential region, indicating the complete filling of trap states. As shown in Fig. 3e and f, V_{TFL} for the control and SF-treated PVK films was measured to be 0.92 V and 0.67 V, respectively. The corresponding defect densities (N_t) for these films were calculated to be 8.63×10^{15} cm^{-3} and 6.22×10^{15} cm^{-3}, respectively. The significant reduction in defect state density after SF treatment demonstrates that the synergistic passivation effect of the disulfide group and the two fluorine groups in the molecule can effectively passivate charged defects in the perovskite.[55] This is a key factor contributing to the achievement of an open-circuit voltage of 1.17 V, which is consistent with the results obtained from TRPL measurements.

To quantitatively evaluate voltage losses, we employed photoluminescence quantum yield (PLQY) to compare charge-carrier recombination rates in the presence and absence of an interlayer, both before and after C_{60} deposition (Fig. S12). The unpassivated perovskite exhibited a PLQY of 0.91%, whereas surface functionalization SF treatment increased the PLQY to 2.25% (See Table S3). The voltage loss difference between samples with and without the C_{60} was 77 mV for the control

device, but decreased to 60 mV for the SF-treated device. This reduction demonstrates that the introduction of the SF interlayer effectively mitigates non-radiative recombination at the interfacial region.[15,56–60]

The overall evidence supports a dual-passivation mechanism introduced by SF molecules: sulfur atoms coordinate with under-coordinated Pb^{2+} *via* Pb–S bonding, while fluorine atoms form hydrogen bonds with organic cations (FA^+/MA^+) and suppress halide vacancies. This action not only reduces trap densities and enhances charge transport but also improves environmental durability. The hydrophobic fluorinated phenyl rings in SF further act as a moisture barrier.

PL spectra (Fig. 3g) reveal that the emission peak of the control sample is red-shifted by 17 nm compared to the SF-treated film, corresponding to a shallow trap energy level $E_t \approx E_c - 0.033$ eV. This suggests that in the control sample, photo-generated carriers undergo comparatively more significant trap-assisted (band-to-defect) recombination.[61] Upon the introduction of SF molecules, this trap-assisted recombination is suppressed, indicating effective passivation of shallow traps and suppression of non-radiative pathways (Fig. 4b).

To further substantiate this, stroboSCAT measurements were conducted to resolve carrier diffusion behavior in real time.[62,63] In Fig. 4a, We present a diagram illustrating the investigation of carrier migration dynamics in perovskite thin films.[64] Here we excited the sample with a 440 nm light pulse (~100 ps pulse) focused to a 209 nm (the pump reflection size) spot size (full width at half maximum). The pump laser fluence is 2.2 or 4.2 μJ cm^{-2} for all measurements. To confirm that both fluences are within the linear regime, *i.e.*, we don't see the effect of strong carrier–carrier interactions in Fig. S14. The resulting excited carrier profile was imaged using a time-delayed widefield 705 nm probe light pulse (~100 ps pulse). The image contrast is proportional to the carrier induced changes to the material's refractive index. Comparing images at different pump–probe time delays to dark reference images gives the spatiotemporal transient reflectance images, $\Delta R/R$. We fit the radial expansion of the carrier distribution to a Gaussian profile of width σ over time t to find the mean-squared expansion, $\sigma^2(t) - \sigma^2(0)$. The spatial broadening of the photo-generated carrier distribution was analyzed using the diffusion model:[65]

$$\sigma^2(t) - \sigma^2(0) = 2Dt^{\alpha}$$

where $\sigma^2(t)$ represents the variance of the Gaussian spatial profile at time t, D is the diffusion coefficient, and α is a constant characterizing the carrier diffusion behavior ($\alpha = 1$ indicates a diffusive model while $\alpha < 1$ indicates a subsidiffusive model).[66] From the sequential stroboSCAT images shown in Fig. 4c, time-resolved Gaussian fitting of the carrier distribution

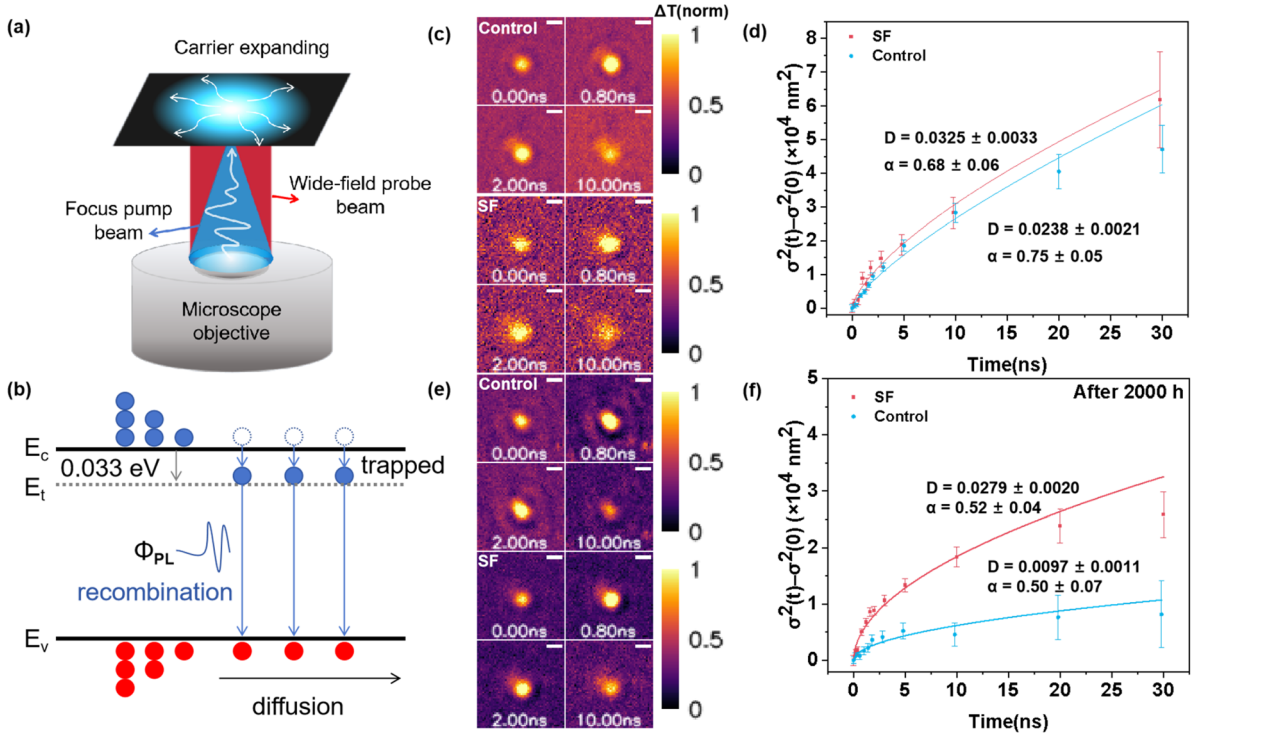

Fig. 4 Carrier diffusion in perovskite films. (a) Schematic diagram of how stroboSCAT studies carrier transport. (b) Schematic illustration of the carrier diffusion and recombination processes in perovskite films. (c) Representative stroboSCAT time series about the carrier transport process from in control and SF-modified perovskite films. (d) Mean squared displacement (m.s.d.) for the data shown in panel (c), obtained through Gaussian fits to the expanding carrier distribution. Error bars represent standard deviations derived from Gaussian fits. (e) Representative stroboSCAT time series about carrier transport process for perovskite films with and without SF modification, stored for more than 2000 hours. Maximum intensities are normalized to 1 by multiplying with the factors shown in the images. (f) m.s.d. for the data shown in panel (e) obtained through Gaussian fits to the expanding carrier distribution. Error bars represent standard deviations derived from Gaussian fits. Scale bar in panel (c) and (e): 500 nm.

was performed, and the results are presented in Fig. 4d. Fitting the experimental data yields a diffusion coefficient (D) of 0.0325 ± 0.0033 $cm^2\ s^{-1}$ for the SF-treated films, representing a 37% enhancement compared to the control group (0.0238 ± 0.0021 $cm^2\ s^{-1}$). This improvement indicates enhanced carrier diffusion coefficient and reduced defect density. The results from multiple characterization techniques demonstrate that SF passivation effectively reduces defect density (SCLC measurement), leading to enhanced carrier transport. Key improvements include reduced trap density, increased PL intensity, extended carrier lifetimes, smoother surface potential, and improved PLQY, all of which support the conjecture of more efficient material performance.

Gaussian fitting of the time-resolved carrier distribution was conducted based on the sequential stroboSCAT images in Fig. 4e, with the fitting results illustrated in Fig. 4f. To evaluate long-term operational robustness, samples were stored under ambient conditions for over 2000 hours. The carrier diffusion coefficient in the control group decreased from 0.0238 ± 0.0021 $cm^2\ s^{-1}$ to 0.0097 ± 0.0011 $cm^2\ s^{-1}$, retaining only 41% of its initial value (Fig. 5a). In contrast, the SF-modified films maintained 86% of their initial maximum diffusion coefficient (0.0325 ± 0.0033 $cm^2\ s^{-1}$ to 0.0279 ± 0.0020 $cm^2\ s^{-1}$) (Fig. 5a). Three months later, the maximum carrier diffusion coefficient of the SF sample was 2.88 times higher than that of the Control sample (0.0279 ± 0.0020 $cm^2\ s^{-1}$ *vs.* 0.0097 ± 0.0011 $cm^2\ s^{-1}$), showcasing excellent carrier transport stability (Fig. 4c–f). This is well correlated with PCE retention: the SF device retained 96.8%, while the control device dropped to 60% after aging (Fig. 5e).

In the previous section, we focused on the maximum carrier diffusion coefficient of the samples. To further validate the reliability of our carrier diffusion coefficient measurements and their consistency with the overall stability of device parameters in perovskite solar cells, we conducted an extensive set of stroboSCAT experiments (Fig. 5a). For each listed sample, five independent measurement of carrier diffusion at different sample locations were performed with stroboSCAT, and the resulting diffusion coefficient is summarized in Fig. 5a. In this context, the average carrier diffusion coefficient provides a more comprehensive evaluation of transport behavior, as it is derived from 20 independent measurements, each based on the mean of three time-resolved scans. This multi-trial approach enhances the statistical reliability of the data and offers a representative characterization of the overall carrier transport properties of the material. We compared the average diffusion coefficient values of SF-treated and control perovskite films, both initially and after 2000 hours of ambient storage. Initially, the SF sample exhibited an average diffusion coefficient of 0.0289 ± 0.0028 $cm^2\ s^{-1}$, which is 35.0% higher than that of the control sample (0.0214 ± 0.0013 $cm^2\ s^{-1}$). After 2000 hours, this difference became even more pronounced: the SF film retained a diffusion coefficient of 0.0247 ± 0.0028 $cm^2\ s^{-1}$, while the control sample declined significantly to 0.0079 ± 0.0017 $cm^2\ s^{-1}$. This means the SF sample preserved 85% of its initial diffusion coefficient, in stark contrast to only 37% retention in

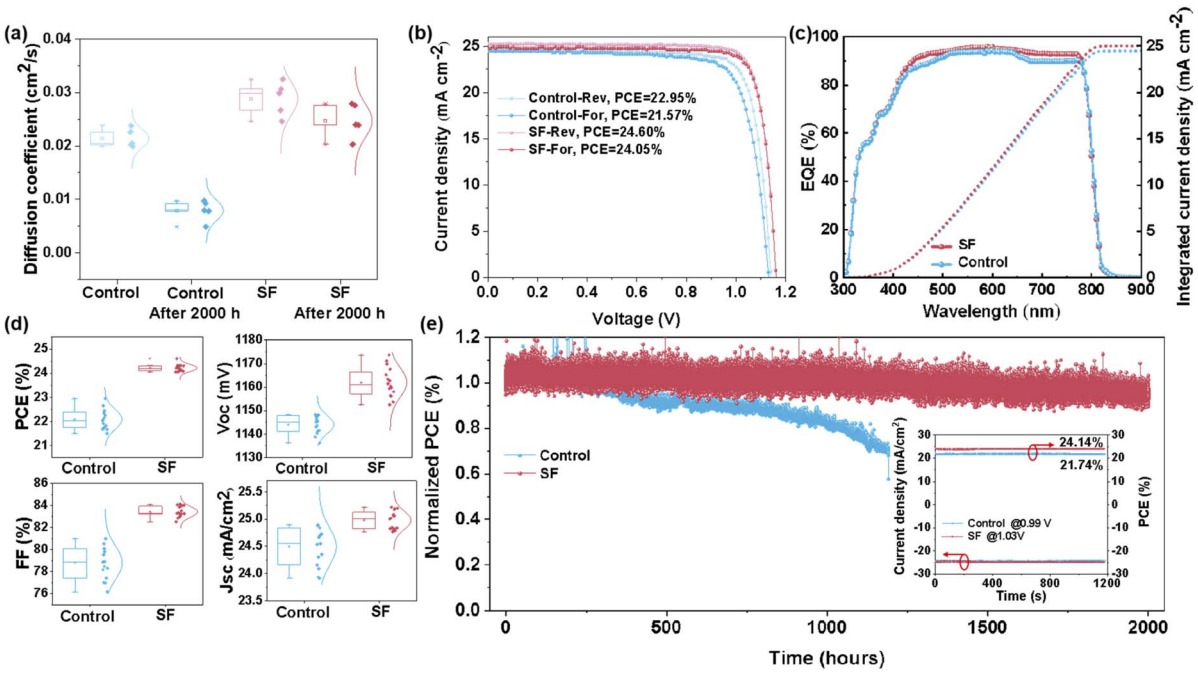

Fig. 5 (a) Statistical distribution of diffusion coefficients in perovskite films, extracted by fitting time-series carrier diffusion profiles from 20 sets of stroboSCAT measurements. The data can represent the average carrier diffusion coefficient levels of the whole perovskite films: SF-treated and untreated films, both before and after 2000 hours of storage. (b) I–V curves of the champion perovskite solar cells with and without SF treatment. (c) EQE spectra and the corresponding integrated J_{sc} of the champion PSCs. (d) Statistical distribution of performance for PSCs integrated with and without SF-treated perovskite films. (e) Operational stability of control, and SF-treated perovskite solar cells, and the inset shows the control and SF-treated corresponding stabilized PCE.

the control. Notably, the average carrier diffusion coefficient of the SF sample after three months was ~3 times that of the control sample, underscoring the long-term transport stability conferred by the SF modification.

This pronounced enhancement in carrier transport stability is closely aligned with the superior device performance observed in SF-treated solar cells. As shown in Fig. 5c, the EQE spectra and integrated current density curves reveal stronger photoresponse in surface-modified devices. The integrated current densities of the control and SF-treated devices were 24.48 mA cm^{-2} and 25.01 mA cm^{-2}, respectively, in good agreement with the light J-V characteristics.

To further assess the effect of surface modification on device stability, we subjected both control and SF-treated cells to maximum power point (MPP) tracking under continuous AM 1.5G illumination (100 mW cm^{-2}). The SF-treated devices exhibited outstanding operational stability, retaining 96.8% of their initial power conversion efficiency (PCE) after 2000 hours of light soaking. In contrast, the control devices experienced a >40% efficiency drop after just 1200 hours (Fig. 5e), confirming the effectiveness of SF passivation in stabilizing p-i-n PSCs. The outstanding stability was attributed to the SF-treated devices' enhanced humidity stability, driven by a significant reduction in defect state density and the presence of hydrophobic functional groups (*e.g.*, fluorine and phenyl rings).[36] Additionally, improvements in perovskite film orientation and strong hydrogen bonding interactions[28] (N–H···F) effectively anchored the organic cations, leading to a marked increase in device stability. In addition, it was observed that the SF-treated perovskite film still shows a stable black phase after being placed under ambient condition for 3 months (Fig. S15).

To further investigate the impact of surface modification on the photovoltaic performance of the devices, a series of perovskite solar cells with the structure ITO/Poly-4PACz/$MA_{0.7}FA_{0.30}$-PbI_3/SF/C_{60}/BCP/Cu were integrated. Fig. 5b, d and Table 1 summarize the light *J–V* curves and corresponding detailed photovoltaic parameters of perovskite film integrated PSCs before and after SF modification. The champion efficiency of the control group device is 22.95%, with an open-circuit voltage (V_{oc}) of 1.14 V, a short-circuit current density (J_{sc}) of 24.84 mA cm^{-2}, and a fill factor (FF) of 80.96%. After SF surface treatment, the device performance improved, achieving a champion efficiency of 24.60%, with V_{oc}, J_{sc}, and FF values of 1.17 V, 25.01 mA cm^{-2}, and 84.07%, respectively. In p-i-n devices fabricated by blade coating under ambient air using Cu as the counter electrode, both PCE and V_{oc} are a decently high levels. The enhanced device performance stems from effective interface engineering, where the SF treatment reduces interfacial defect recombination and optimizes energy alignment, suppressing non-radiative recombination. This yields a 20 mV V_{oc} increase (1.16 V on average) due to improved quasi-Fermi level splitting (from 1.134 V to 1.149 V, Fig. S12),[67] while simultaneously boosting J_{sc} and FF through more efficient charge transfer. The collective improvements in V_{oc}, FF, and J_{sc} – attributed to superior defect passivation, recombination suppression, and energy level matching – synergistically enhance the overall PCE.

The champion device further shows a stabilized PCE of 24.14% (SF-treated), while the control device achieves 21.74% (Fig. 5e). The SF-treated solar cell exhibits negligible hysteresis (Fig. 5b), with the hysteresis index (HI) decreasing from 0.06 (control solar cell) to 0.02 (SF-treated solar cell), attributed to suppressed ion migration and interfacial trap states,[13] better-matched energy levels reducing charge accumulation, along with improved interfacial connectivity and carrier extraction.[12]

Table 1 Photovoltaic parameters of the perovskite solar cells integrated with control and SF-treated perovskite films. The average parameters and standard deviation values were calculated based on measurements from 16 devices

Device	V_{oc} (V)	J_{sc} (mA cm^{-2})	FF (%)	PCE (%)
Control	1.14 ± 0.04 (1.14)	24.55 ± 0.40 (24.84)	78.88 ± 1.49 (80.96)	22.14 ± 0.47 (22.95)
SF-treated	1.16 ± 0.006 (1.17)	24.98 ± 0.16 (25.01)	83.37 ± 0.44 (84.07)	24.20 ± 0.11 (24.60)

Conclusion

This study demonstrates bis(3-fluorophenyl)disulfide (SF) as a multi-functional passivator for planar perovskite solar cells (PSCs), effectively addressing interfacial defects and energy-level mismatches at the PVK/ETL interface. The disulfide-linked bifunctional structure of SF enables dual-site passivation: sulfur atoms coordinate with undercoordinated Pb^{2+} *via* Pb–S bonds, while fluorine atoms occupy iodine vacancies and form hydrogen bonds with FA^+/MA^+ cations. This reduces both deep and shallow trap states, as well as suppresses ion migration. Notably, this defect suppression leads to significantly improved carrier transport efficiency and stability. StroboSCAT and TRPL measurements reveal that SF-modified films retain 86% of their initial carrier diffusion coefficient (0.0325 ± 0.0033 cm^2 s^{-1} to 0.0279 ± 0.0020 cm^2 s^{-1}) after 2000 h in ambient air, while controls retain only 41%. This enhancement in the carrier diffusion coefficient directly contributes to the long-term operational robustness of PSCs. As a result, devices incorporating SF (ITO/Poly-4PACz/$MA_{0.7}FA_{0.30}$-PbI_3/SF/C_{60}/BCP/Cu) achieve a high power conversion efficiency (PCE) of 24.60% and a V_{oc} of 1.17 V. Encapsulated SF-based devices retain 96.8% of initial PCE after 2000 hours at 30–40% relative humidity, outperforming control devices (60% retention after 1200 hours). The hydrophobic fluorinated aromatic rings in SF further contribute to moisture resistance. The proposed SF enables efficient and stable carrier transport by reducing trap densities and suppressing ion migration, thereby facilitating durable and high-efficiency PSCs, demonstrating a promising strategy for stable and efficient ambient-air blade-coating fabrication.

Author contributions

Jian-An Li and Hailong Ma contributed to the experimental conceptualization, data curation, visualization, manuscript writing, and editing. Xiangpeng Ding performed the theoretical calculations. Shuyan Chen conducted solar cell stability tracking. Shuoren Li, Bin Han, Wangxian Chen, Sihao Huang, Yuelin Kuang, and Zixi Liu contributed to validation. Chang

Yan supervised the project, administered its execution, and reviewed and revised the manuscript.

Conflicts of interest

There are no conflicts to declare.

Data availability

The data supporting this article have been included as part of the SI.

Chemical materials used in this research; device fabrication; measurements and characterizations; calculations. See DOI: https://doi.org/10.1039/d5ta04703j.

Acknowledgements

This work was supported by the National Natural Science Foundation of China (No. 62204067), Guangdong-Hong Kong Joint Laboratory for Carbon Neutrality (Funding code: 2023B1212120003), Guangdong provincial project 2023QN10L076 and Guangdong-Hong Kong Universities "1+1+1" Joint Funding Program (P00538, G01MF000014). The authors acknowledged the Materials Characterization and Preparation Facility (GZ) of the Hong Kong University of Science and Technology (Guangzhou) for their technical support. We also acknowledge the facility and service support from the Laboratory for Brilliant Energy Science and Technology (BEST) Lab and Green e Materials (GeM) Lab at the Hong Kong University of Science and Technology (Guangzhou).

References

1 L. Wu, S. Hu, F. Yang, G. Li, J. Wang, W. Zuo, J. J. Jerónimo-Rendon, S.-H. Turren-Cruz, M. Saba, M. Saliba, M. K. Nazeeruddin, J. Pascual, M. Li and A. Abate, *Nat. Rev. Mater.*, 2025, **10**, 536–549.
2 Z. Zhang, L. Qiao, K. Meng, R. Long, G. Chen and P. Gao, *Chem. Soc. Rev.*, 2023, **52**, 163–195.
3 Y. Ma and Q. Zhao, *J. Energy Chem.*, 2022, **64**, 538–560.
4 M. Younas, T. A. Kandiel, A. Rinaldi, Q. Peng and A. A. Al-Saadi, *Mater. Today Phys.*, 2021, **21**, 100557.
5 D. Devadiga, M. Selvakumar, P. Shetty and M. S. Santosh, *J. Power Sources*, 2021, **493**, 229698.
6 Z. Ren, Z. Cui, X. Shi, L. Wang, Y. Dou, F. Wang, H. Lin, H. Yan and S. Chen, *Joule*, 2023, **7**, 2894–2904.
7 T. Danielyan, A. Asatryan, A. Sahakyan and H. Khachatryan, *J. Power Sources*, 2025, **630**, 235995.
8 Q. Cao, Y. Wang, X. Xiang, J. Yu and J. Zhou, *ACS Sustain. Chem. Eng.*, 2025, **13**, 5079–5090.
9 Z. Zhao, W. Liu, T. Kong, Y. Liu, W. Chen, P. Gao and D. Bi, *Adv. Funct. Mater.*, 2025, **35**, 2419393.
10 T. Liu, Z. Ren, Y. Liu, Y. Zhang, J. Liang, F. Cheng, Y. Li, X. Shi, Y. Dou, X. Hu, L. Wang, S. Luo, F. Wang, X. Peng, Y. Zhao, W. Wang, Y. Cao, F. Gao and S. Chen, *Sci. Adv.*, 2025, **11**, eadu3493.
11 Z. Ni, C. Bao, Y. Liu, Q. Jiang, W.-Q. Wu, S. Chen, X. Dai, B. Chen, B. Hartweg, Z. Yu, Z. Holman and J. Huang, *Science*, 2020, **367**, 1352–1358.
12 J. H. Heo, H. J. Han, D. Kim, T. K. Ahn and S. H. Im, *Energy Environ. Sci.*, 2015, **8**, 1602–1608.
13 S. van Reenen, M. Kemerink and H. J. Snaith, *J. Phys. Chem. Lett.*, 2015, **6**, 3808–3814.
14 X. Chu, Q. Ye, Z. Wang, C. Zhang, F. Ma, Z. Qu, Y. Zhao, Z. Yin, H.-X. Deng, X. Zhang and J. You, *Nat. Energy*, 2023, **8**, 372–380.
15 D. Shi, V. Adinolfi, R. Comin, M. Yuan, E. Alarousu, A. Buin, Y. Chen, S. Hoogland, A. Rothenberger, K. Katsiev, Y. Losovyj, X. Zhang, P. A. Dowben, O. F. Mohammed, E. H. Sargent and O. M. Bakr, *Science*, 2015, **347**, 519–522.
16 G. Fu, D.-K. Lee, C. Ma and N.-G. Park, *ACS Energy Lett.*, 2023, **8**, 4563–4571.
17 L. Zhu, X. Zhang, M. Li, X. Shang, K. Lei, B. Zhang, C. Chen, S. Zheng, H. Song and J. Chen, *Adv. Energy Mater.*, 2021, **11**, 2100529.
18 H. Su, Z. Xu, X. He, Y. Yao, X. Zheng, Y. She, Y. Zhu, J. Zhang and S. Liu, *Adv. Mater.*, 2023, **36**, 2306724.
19 R. Wang, A. Altujjar, N. Zibouche, X. Wang, B. F. Spencer, Z. Jia, A. G. Thomas, M. Z. Mokhtar, R. Cai, S. J. Haigh, J. M. Saunders, M. S. Islam and B. R. Saunders, *Energy Environ. Sci.*, 2023, **16**, 2646–2657.
20 L. Yan, H. Huang, P. Cui, S. Du, Z. Lan, Y. Yang, S. Qu, X. Wang, Q. Zhang, B. Liu, X. Yue, X. Zhao, Y. Li, H. Li, J. Ji and M. Li, *Nat. Energy*, 2023, **8**, 1158–1167.
21 X. Li, J. Yang, Q. Jiang, W. Chu, D. Zhang, Z. Zhou and J. Xin, *ACS Appl. Mater. Interfaces*, 2017, **9**, 41354–41362.
22 H. Zhu, Y. Ren, L. Pan, O. Ouellette, F. T. Eickemeyer, Y. Wu, X. Li, S. Wang, H. Liu, X. Dong, S. M. Zakeeruddin, Y. Liu, A. Hagfeldt and M. Grätzel, *J. Am. Chem. Soc.*, 2021, **143**, 3231–3237.
23 X. Ding, H. Wang, Y. Miao, C. Chen, M. Zhai, C. Yang, B. Wang, Y. Tian and M. Cheng, *ACS Appl. Mater. Interfaces*, 2022, **14**, 3930–3938.
24 C. Tian, Y. Zhao, X. Han, B. Li, Y. Rui, H. Xiong, Y. Qiu, W. An, K. Li, C. Hou, Y. Li, H. Wang and Q. Zhang, *Chem. Eng. J.*, 2023, **452**, 139345.
25 C. Jiang, N. Li, Y. Niu, N. Liu, D. Li, G. Jin, Y. Zhong, X. Tao and Z. Chen, *Angew. Chem., Int. Ed.*, 2024, **63**, e202412485.
26 B. Chen, P. N. Rudd, S. Yang, Y. Yuan and J. Huang, *Chem. Soc. Rev.*, 2019, **48**, 3842–3867.
27 Y.-H. Lin, F. Vikram, X.-L. Cao, A. Dasgupta, R. D. J. Oliver, A. M. Ulatowski, M. M. McCarthy, X. Shen, Q. Yuan, M. G. Christoforo, F. S. Y. Yeung, M. B. Johnston, N. K. Noel, L. M. Herz, M. S. Islam and H. J. Snaith, *Science*, 2024, **384**, 767–775.
28 N. Chen, X. Huang, Y. Gao, P. Gao and Q.-S. Li, *J. Phys. Chem. Lett.*, 2024, **15**, 12282–12292.
29 J. Zhang, Z. Li, F. Guo, H. Jiang, W. Yan, C. Peng, R. Liu, L. Wang, H. Gao, S. Pang and Z. Zhou, *Angew. Chem., Int. Ed.*, 2023, **62**, e202305221.
30 C. Liu, H. Su, Y. Pu, M. Guo, P. Zhai, Z. Liu and Z. Zhang, *Nano Energy*, 2023, **118**, 108990.

31 M. Delor, H. L. Weaver, Q. Yu and N. S. Ginsberg, *Nat. Mater.*, 2020, **19**(1), 56–62.
32 I. S. Zhidkov, D. W. Boukhvalov, A. F. Akbulatov, L. A. Frolova, L. D. Finkelstein, A. I. Kukharenko, S. O. Cholakh, C.-C. Chueh, P. A. Troshin and E. Z. Kurmaev, *Nano Energy*, 2021, **79**, 105421.
33 Q. Cao, T. Wang, X. Pu, X. He, M. Xiao, H. Chen, L. Zhuang, Q. Wei, H. L. Loi, P. Guo, B. Kang, G. Feng, J. Zhuang, G. Feng, X. Li and F. Yan, *Adv. Mater.*, 2024, **36**, 2311970.
34 C. Liu, Y. Yang, H. Chen, I. Spanopoulos, A. S. R. Bati, I. W. Gilley, J. Chen, A. Maxwell, B. Vishal, R. P. Reynolds, T. E. Wiggins, Z. Wang, C. Huang, J. Fletcher, Y. Liu, L. X. Chen, S. De Wolf, B. Chen, D. Zheng, T. J. Marks, A. Facchetti, E. H. Sargent and M. G. Kanatzidis, *Nature*, 2024, **633**, 359–364.
35 Z. Feng, Y. Wang, J. Si, J. Xu, Y. Guo, H. Huang, Y. Ji, H. Zhang, L. Li, S. Kang, X. Wu, X. Li, Y. Peng, Y. Liu, C. Ge, C. Huang, Y. Zhang, J. Sun, S. Chen, W. Zhou, D. Tang, Y. Li, B. Ding, J. Z. Liu, K. Weber, N. Hu, X. He, Y. Cui, H. Zhan, X. Zhang and J. Peng, *Adv. Energy Mater.*, 2025, 2502409.
36 T. Li, J. Xu, R. Lin, S. Teale, H. Li, Z. Liu, C. Duan, Q. Zhao, K. Xiao, P. Wu, B. Chen, S. Jiang, S. Xiong, H. Luo, S. Wan, L. Li, Q. Bao, Y. Tian, X. Gao, J. Xie, E. H. Sargent and H. Tan, *Nat. Energy*, 2023, **8**, 610–620.
37 X. Zhou, J. Wu, J. Zeng, D. Wang, J. Chen, M. Zhang, W. Peng, Z. Liu, Y. Zhang, L. Zhang, L. Yan, C. Liu, X. Wang and B. Xu, *Nano Energy*, 2024, **130**, 110170.
38 N. Li, S. Tao, Y. Chen, X. Niu, C. K. Onwudinanti, C. Hu, Z. Qiu, Z. Xu, G. Zheng, L. Wang, Y. Zhang, L. Li, H. Liu, Y. Lun, J. Hong, X. Wang, Y. Liu, H. Xie, Y. Gao, Y. Bai, S. Yang, G. Brocks, Q. Chen and H. Zhou, *Nat. Energy*, 2019, **4**, 408–415.
39 H. Cui, Q. Zhang, Y. Bo, P. Bai, M. Wang, C. Zhang, X. Qian and R. Ma, *Joule*, 2022, **6**, 258–268.
40 M. Wu, Y. Duan, L. Yang, P. You, Z. Li, J. Wang, H. Zhou, S. Yang, D. Xu, H. Zou and Z. Liu, *Adv. Funct. Mater.*, 2023, **33**, 2300128.
41 L. Yang, J. Feng, Z. Liu, Y. Duan, S. Zhan, S. Yang, K. He, Y. Li, Y. Zhou, N. Yuan, J. Ding and S. Liu, *Adv. Mater.*, 2022, **34**, 2201681.
42 L. Wang, J. Xia, Z. Yan, P. Song, C. Zhen, X. Jiang, G. Shao, Z. Qiu, Z. Wei, J. Qiu and M. K. Nazeeruddin, *Adv. Funct. Mater.*, 2022, **32**, 2204725.
43 J.-W. Lee, H.-S. Kim and N.-G. Park, *Acc. Chem. Res.*, 2016, **49**, 311–319.
44 F. Ye, S. Zhang, J. Warby, J. Wu, E. Gutierrez-Partida, F. Lang, S. Shah, E. Saglamkaya, B. Sun, F. Zu, S. Shoaee, H. Wang, B. Stiller, D. Neher, W.-H. Zhu, M. Stolterfoht and Y. Wu, *Nat. Commun.*, 2022, **13**, 7454.
45 H. Chen, S. Teale, B. Chen, Y. Hou, L. Grater, T. Zhu, K. Bertens, S. M. Park, H. R. Atapattu, Y. Gao, M. Wei, A. K. Johnston, Q. Zhou, K. Xu, D. Yu, C. Han, T. Cui, E. H. Jung, C. Zhou, W. Zhou, A. H. Proppe, S. Hoogland, F. Laquai, T. Filleter, K. R. Graham, Z. Ning and E. H. Sargent, *Nat. Photonics*, 2022, **16**, 352–358.
46 H. Chen, A. Maxwell, C. Li, S. Teale, B. Chen, T. Zhu, E. Ugur, G. Harrison, L. Grater, J. Wang, Z. Wang, L. Zeng, S. M. Park, L. Chen, P. Serles, R. A. Awni, B. Subedi, X. Zheng, C. Xiao, N. J. Podraza, T. Filleter, C. Liu, Y. Yang, J. M. Luther, S. De Wolf, M. G. Kanatzidis, Y. Yan and E. H. Sargent, *Nature*, 2022, **613**, 676–681.
47 F. Li, X. Deng, F. Qi, Z. Li, D. Liu, D. Shen, M. Qin, S. Wu, F. Lin, S.-H. Jang, J. Zhang, X. Lu, D. Lei, C.-S. Lee, Z. Zhu and A. K. Y. Jen, *J. Am. Chem. Soc.*, 2020, **142**, 20134–20142.
48 S. Panigrahi, T. Calmeiro, M. J. Mendes, H. Águas, E. Fortunato and R. Martins, *J. Phys. Chem. C*, 2022, **126**, 19367–19375.
49 J. J. Li, J. Y. Ma, Q. Q. Ge, J. S. Hu, D. Wang and L. J. Wan, *ACS Appl. Mater. Interfaces*, 2015, **7**, 28518–28523.
50 X. Feng, C. Li, J. Song, Y. He, W. Qu, W. Li, K. Guo, L. Liu, B. Yang and H. Wei, *Nat. Commun.*, 2024, **15**, 577.
51 Y. Wei, S. Wang, M. Chen, J. Han, G. Yang, Q. Wang, J. Di, H. Li, W. Wu and J. Yu, *Adv. Mater.*, 2024, **36**, e2302912.
52 G. Delport, S. Macpherson and S. D. Stranks, *Adv. Energy Mater.*, 2020, **10**, 1903814.
53 W. Zhang, C. Xing, W. Song, J. Xie, H. Guan, J. Shan, J. Zhu, M. Yang and Z. Ge, *Adv. Mater.*, 2025, e2503954, DOI: **10.1002/adma.202503954**.
54 X. Liu, R. Liu, J. Qiu, X. Cheng and G. Li, *Angew Chem. Int. Ed. Engl.*, 2020, **59**, 13962–13967.
55 K. Xiao, Q. Han, Y. Gao, S. Gu, X. Luo, R. Lin, J. Zhu, J. Xu and H. Tan, *J. Energy Chem.*, 2021, **56**, 455–462.
56 C. Luo, G. Zheng, F. Gao, X. Wang, C. Zhan, X. Gao and Q. Zhao, *Nat. Photonics*, 2023, **17**, 856–864.
57 D. Luo, R. Su, W. Zhang, Q. Gong and R. Zhu, *Nat. Rev. Mater.*, 2019, **5**, 44–60.
58 S. D. Stranks, V. M. Burlakov, T. Leijtens, J. M. Ball, A. Goriely and H. J. Snaith, *Phys. Rev. Appl.*, 2014, **2**, 034007.
59 Z. Liu, H. Li, Z. Chu, R. Xia, J. Wen, Y. Mo, H. Zhu, H. Luo, X. Zheng, Z. Huang, X. Luo, B. Wang, X. Zhang, G. Yang, Z. Feng, Y. Chen, W. Kong, J. Gao and H. Tan, *Adv. Mater.*, 2024, **36**, 2308370.
60 M. Stolterfoht, C. M. Wolff, J. A. Márquez, S. Zhang, C. J. Hages, D. Rothhardt, S. Albrecht, P. L. Burn, P. Meredith, T. Unold and D. Neher, *Nat. Energy*, 2018, **3**, 847–854.
61 Y. Rongfeng, R. D. Trevor, B. M. Rafaela, C. A. Alexander, P. H. Ha, Y. Chang, O. C. Justin, K. Siamak, M. J. David, X. Ke, A. A. Paul and G. S. Naomi, *Sci. Adv.*, 2023, **9**, eadh2410.
62 H. Su, D. Xu, S. W. Cheng, B. Li, S. Liu, K. Watanabe, T. Taniguchi, T. C. Berkelbach, J. C. Hone and M. Delor, *Nano Lett.*, 2022, **22**, 2843–2850.
63 H. L. Weaver, C. M. Went, J. Wong, D. Jasrasaria, E. Rabani, H. A. Atwater and N. S. Ginsberg, *ACS Nano*, 2023, **17**, 19011–19021.
64 Y. Ye, Y. Genghua, A. Samah, R. Uwe and K. Thomas, *Sci. Adv.*, 2025, **11**, eadt1171.
65 M. Delor, H. L. Weaver, Q. Yu and N. S. Ginsberg, *Nat. Mater.*, 2020, **19**, 56–62.

66 M. Delor, A. H. Slavney, N. R. Wolf, M. R. Filip, J. B. Neaton, H. I. Karunadasa and N. S. Ginsberg, *ACS Energy Lett.*, 2020, **5**, 1337–1345.
67 Y. Zhao, I. Yavuz, M. Wang, M. H. Weber, M. Xu, J.-H. Lee, S. Tan, T. Huang, D. Meng, R. Wang, J. Xue, S.-J. Lee, S.-H. Bae, A. Zhang, S.-G. Choi, Y. Yin, J. Liu, T.-H. Han, Y. Shi, H. Ma, W. Yang, Q. Xing, Y. Zhou, P. Shi, S. Wang, E. Zhang, J. Bian, X. Pan, N.-G. Park, J.-W. Lee and Y. Yang, *Nat. Mater.*, 2022, **21**, 1396–1402.

